BLUE EMITTING FIBER LASER

Todd E. Weist, Capt, USAF, Daniel S. Hinkel, Lt, USAF and
Kevin Whitcomb, Lt, USAF

APPROVED FOR PUBLIC RELEASE; DISTRIBUTION UNLIMITED.
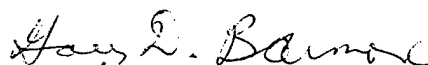
19980415 097

**AIR FORCE RESEARCH LABORATORY
ROME RESEARCH SITE
ROME, NEW YORK**

DTIC QUALITY INSPECTED 3

This report has been reviewed by the Air Force Research Laboratory, Information Directorate, Public Affairs Office (IFOIPA) and is releasable to the National Technical Information Service (NTIS). At NTIS it will be releasable to the general public, including foreign nations.

RL-TR-97-197 has been reviewed and is approved for publication.

APPROVED:

GARY D. BARMORE, Maj., USAF
Chief, Photonics Division

FOR THE DIRECTOR:

DONALD W. HANSON, Director
Surveillance & Photonics Directorate

REPORT DOCUMENTATION PAGE

1. AGENCY USE ONLY (Leave blank)	2. REPORT DATE FEBRUARY 1998	3. REPORT TYPE AND DATES COVERED FINAL, Mar 96 - Sep 97 (In-House)

4. TITLE AND SUBTITLE

BLUE EMITTING FIBER LASER

5. FUNDING NUMBERS

C - NA
PE - 61102F/62702F
PR - 2300/4600
TA - O6/P1
WU - 01 /31

6. AUTHOR(S)

Capt Todd E. Wiest, Lt Daniel S. Hinkel, Lt Kevin Whitcomb

7. PERFORMING ORGANIZATION NAME(S) AND ADDRESS(ES)

Rome Laboratory/OCPA
25 Electronic Pky
Rome NY 13441-4515

8. PERFORMING ORGANIZATION REPORT NUMBER

RL-TR-97-197

9. SPONSORING / MONITORING AGENCY NAME(S) AND ADDRESS(ES)

Rome Laboratory   Department of Defense
26 Electronic Pky   BMDO/TRI
Rome NY 13441-4514   Washington DC 20301-7100

10. SPONSORING / MONITORING AGENCY REPORT NUMBER

RL-TR-97-197

11. SUPPLEMENTARY NOTES

Rome Laboratory Project Engineer: Capt Todd E. Wiest, OCPA, 315-330-7693

12a. DISTRIBUTION AVAILABILITY STATEMENT

APPROVED FOR PUBLIC RELEASE; DISTRIBUTION UNLIMITED

12b. DISTRIBUTION CODE

13. ABSTRACT (Maximum 200 words)

The use of thulium-doped fluorozirconate fiber as a blue laser gain material was studied by investigating the optically active transitions, the optimal laser cavity configuration, and the appropriate gain length when excited by 785 and 1047 nm. Laser-induced fluorescence allowed the thulium energy locations to be determined with a least squares fit producing values for the Slater integrals, $F_2 = 416.52$, $F_4 = 66.5459$, and $F_6 = 5.32902$, and the spin-orbit constant, $\zeta = -1305.51$. Wavelength dependent cross sections and the decay times of recorded transitions were also determined. A model was developed to calculate the small signal gain of the fiber and to compare different cavity configurations. A cut-back experiment produced an optimal fiber length of 2.4 m which differed from the calculation. Also, the trend in the cut-back data does not follow the form predicted by the model. It is believed that spectral competition, which was not included in the model, may explain these deviations. However, the model does show the cavity configuration with both lasers coupled through the back mirror and both mirrors butted to the ends of the fiber as optimal for gain produced and controllability of the blue laser output.

14. SUBJECT TERMS

blue laser, fiber laser, fluorozirconate (ZBLAN), thulium, upconversion

15. NUMBER OF PAGES

44

16. PRICE CODE

17. SECURITY CLASSIFICATION OF REPORT UNCLASSIFIED	18. SECURITY CLASSIFICATION OF THIS PAGE UNCLASSIFIED	19. SECURITY CLASSIFICATION OF ABSTRACT UNCLASSIFIED	20. LIMITATION OF ABSTRACT UNLIMITED

TABLE OF CONTENTS

i

LIST OF FIGURES

LIST OF TABLES

1. Summary

The next major improvement of many optical systems, especially data storage, will occur when lasers are developed with wavelengths shorter than the infrared (IR) and red wavelengths currently used. This improvement will result because of the ability to focus the shorter wavelength light to smaller spot sizes. Due to the large military and civilian market, numerous laboratories and universities are developing blue laser devices.

The substantial amount of research into a compact blue laser source is focused on the development of semiconductor diodes fabricated out of nitride-based material. However, other methods do exist to create blue laser light from a system that is compact. One of these methods, upconversion lasing obtained with a doped fiber gain material, is the subject of this report.

When thulium ions (Tm^{3+}) are doped into fluorozirconate (ZBLAN) fiber, upconversion processes are possible. These processes allow the use of IR pump lasers to produce blue laser emission at 480 nm. Due to the characteristics of the ZBLAN fiber, numerous possible excitation schemes are available and a robust excitation scheme which uses two IR wavelengths will be presented.

The electronic configuration and transitions which are pertinent in the lasing phenomena will be discussed. This will be done by investigating the laser-induced fluorescence from the upper laser level. A method to determine the energy level locations as well as the cross sections for particular transitions will be derived and applied to the fluorescence spectrum recorded. Also, time-dependent fluorescence will be utilized to aid in the assignment of the transitions recorded and the lifetimes of the upper energy level involved in each fluorescence feature.

This data can be used to create a model of the lasing process to determine the amount of gain available from the doped fiber. This was done to determine the optimal length of the fiber gain media. This parameter is important since the 480 nm transition in Tm:ZBLAN fiber is ground state terminated (GST). That is, if the fiber is too long, the population in the ground state will significantly reduce the number of photons at the lasing wavelength; the gain material is lossy at that wavelength. Also, this model can be used to determine the optimal configuration of the cavity. Since fiber is being used as the gain material, coupling the pump light into the fiber is an important consideration. However, as the number of elements intra-cavity increases, so does the cavity loss. With the increase of cavity loss comes the increase in laser threshold, and thus, inefficient operation of the laser.

To ensure the maximum amount of gain is achieved, one uses a long piece of fiber. However, as mentioned above, this transition has inherent loss if the fiber is too long. Hence, experiments were completed to determine the length of fiber which produced the maximum fluorescence power output when excited by the two IR wavelengths determined to produce a robust excitation scheme.

2. Introduction

The development of compact blue lasers has been receiving considerable attention. These devices can be used for applications ranging from data storage and flat displays to inspection systems and flow cytometry. Considerable resources have been expended to develop blue emitting semiconductor laser diodes, however, another compact method of generating blue light is available. This alternative method involves the use of an upconversion process to create visible light in a doped fiber.

The upconversion process is so named because the absorption of multiple excitation photons results in the emission of a single photon that is more energetic than any single photon; the photon energy output is larger than any single photon energy input to the system. This process is possible when excited states of the absorbing material are metastable, i.e., long lived. Once excited to a metastable state, the material can then absorb another photon and be excited to a higher energy state. This process will continue until either a short-lived excited state is encountered or the excitation photons are not resonant with higher energy states of the material. Using this process, infrared (IR) light can be used to excite electronic transitions of rare earth ions to produce emission in the visible spectrum.

The rare earth, also known as lanthanide, ions used in this process are trivalent; there are three electrons removed from the stable element. This oxidation state results in a $5s^2 5p^6$ electronic configuration having lost the $6s$ and one of the $4f$ electrons.[1] The loss of the $4f$ electron allows these ions to be optically active, i.e., the $4f$ electrons change energy state through the absorption and emission of photons. Each energy state has an associated energy level which can be described by the Russel-Saunders labeling scheme for many electron atoms. In this scheme, each energy level has a label of the form $^{2S+1}L_J$ where $2S+1$ is the spin multiplicity of the state, L is the orbital angular momentum, and J is the total angular momentum.[2]

When the ion is introduced into a glass host, the energy states of the ion are perturbed. This perturbation has little effect on the optical properties of the ion since the outer electrons, $5s$ and $5p$, shield the $4f$ electrons from the potential (Ligand) field of the glass.[1] While the free ion energy states are degenerate, i.e., each energy state has $2J+1$ electronic states associated with it, the Ligand field lifts this degeneracy, and the energy states form Stark levels which are separated by only a few meV.[1] With this small separation, the Stark levels are unresolved, and the result is spectrally broad absorption and emission features which have numerous benefits.

By forming the doped glass into fiber, many advantages are obtained. The first is the elimination of optics to achieve the proper mode volume. While a lens is required to couple light into the fiber, all other optics can be planar. At that time, the pump light is confined in the fiber by its waveguiding properties. These properties coupled with the small core sizes of fiber create another advantage: high intensities (1 mW of pump laser power in the core corresponds to a 150 MW/m^2 intensity in the core). Since intensity is the main "driver" in laser operation, high intensity for low pump power is a clear advantage. Another significant advantage fibers have is the ability to select the length of gain material. Since fibers are drawn and not grown (like crystals), any length can be selected as required by the application or determined from the pump laser power. It is this length selection capability that allows the erbium 1.55 µm transition to lase in fiber.

2

2.1 Material Interactions

Fundamental to the utilization of doped fiber is the interaction of the trivalent rare earth ions and light. A simplified diagram of the Tm^{3+} $4f$ electronic energy levels appears in Figure 2-1. In this figure, the upward arrows labeled 1 to 3 are absorption of IR light resulting in the excitation of the electron from
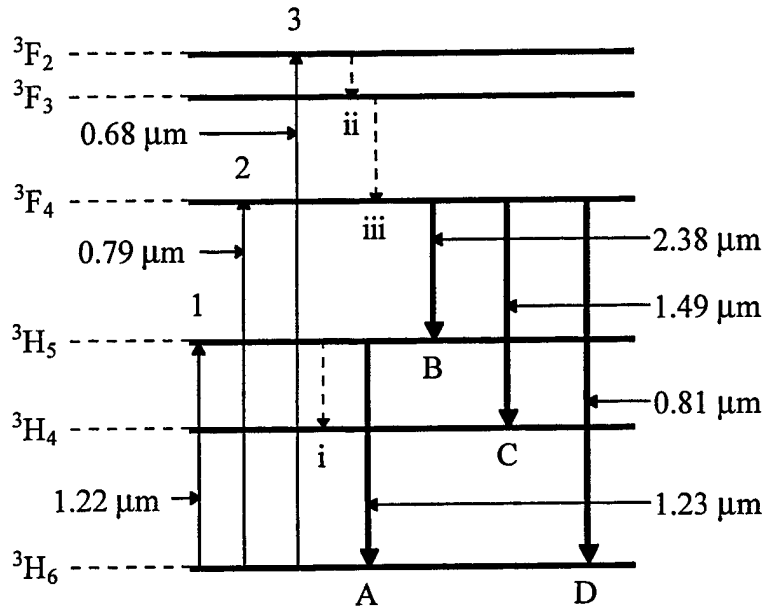
Figure 2-1. Optical transitions and a simplified energy diagram for Tm^{3+}.

the $^3H_6$ level to the $^3H_5$, $^3F_4$, and $^3F_2$, respectively. The bold downward arrows represent the emission, or fluorescence, of light. The transitions shown in Figure 2-1 only contain "normal" phenomena, i.e., the excitation energy is higher than the emission energy.

In fluoride-based fiber, there are numerous emissions available since magnetic dipole and electric quadrapole transitions can also occur, i.e., the ΔJ selection rule does not hold. This is another manifestation of the Ligand field.

Since the host is a glass, each ion site experiences a different host potential; this perturbation causes the electronic states of each ion to be at slightly different energy levels due to the lack of ion site symmetry. This asymmetry increases the spectral broadening of the electronic transitions by moving the center energy of the Stark multiplets.

The downward, dashed arrows, numbered i to iii, in Figure 2-1 are non-radiative decays. These decays correspond to the loss of energy by the electron to the glass host. This energy loss usually occurs in the form of phonons and the energies at which these decays occur is host dependent. Figure 2-2 shows the phonon energy of different host materials. As the phonon energy of the host increases, the probability of a non-radiative decay from one state to another increases and approaches unity if the energy separation of the two states is less than the phonon energy of the host. Also, as this phonon energy increases, the number of states available for "energy storing" to obtain an upconversion process is reduced. Therefore, the creation of an IR-pumped source of blue light must utilize a fiber host that has nominal phonon energy. As can be seen in Figure 2-2, fluorozirconate (made from fluorides of

3

zirconium, barium, lithium, aluminum, and sodium -- a.k.a. ZBLAN) is one such glass host. This host can readily be drawn into fiber, and while fiber-based components, i.e., gratings, couplers, etc., are still not available, the mechanical strength of the fiber has approached that of silica making ZBLAN fiber experiments feasible.
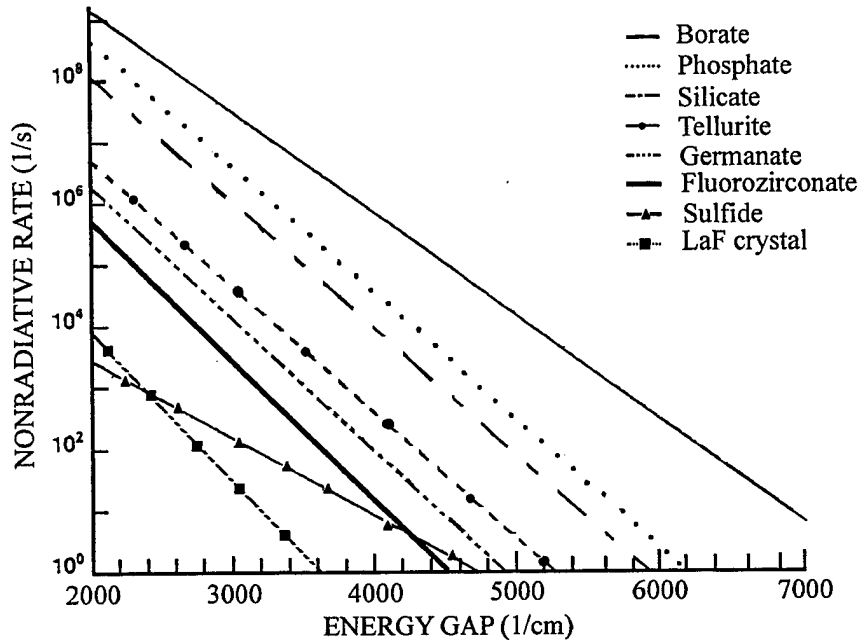
Figure 2-2. Non-radiative relaxation rate as a function of energy gap for the indicated host materials. All materials listed (except LaF crystal) can be drawn into fiber.[3]

With Tm^{3+} doped fluoride fiber, made by exchanging some of the NaF with TmF, upconversion processes are possible to create blue laser emission with high output powers.[4,6] This fiber is mechanically strong and can be protected in ways similar to those used with standard silica fibers. With the development of a blue fiber laser which has greater than 100 mW output (see Ref. 4), it appears possible to create a low power, compact system that could be used in future Air Force optical memory systems.

2.2 Standard Excitation Scheme

At this time, a discussion of the Tm-doped ZBLAN energy levels that are used in the creation of blue light with a single excitation scheme is warranted. The upper laser level for the blue (480 nm) transition is the $^1G_4$ state. Shown in Figure 2-3 is the typical excitation scheme for the creation of blue laser light. In this process, the excitation source is between 1120 - 1160 nm (8621 - 8929 cm^{-1}). This process requires the absorption of three photons ($^3H_6 \rightarrow {}^3H_5$, $^3H_4 \rightarrow {}^3F_3$, and $^3F_4 \rightarrow {}^1G_4$) with two non-radiative decays ($^3H_5 \rightarrow {}^3H_4$ and $^3F_3 \rightarrow {}^3F_4$). By using this pumping scheme, 106 mW of blue laser emission has been recorded.[4] However, this excitation scheme utilizes pump lasers with operational wavelengths greater than 1.1 μm. Compact versions of these lasers are difficult to create and the upconversion process used to create blue light is *very* sensitive to the pump laser wavelength. That is, a

minor deviation in the pump laser wavelength results in a serious degradation of blue laser performance. With these stringent pump laser requirements, diode lasers for a compact system would drive the system cost extremely high. Thus, another upconversion excitation process was sought.

State | Energy (10^3 cm^{-1})

$^1G_4$ ——————— 20.903

$^3F_2$ ——————— 14.176
$^3F_3$ ——————— 14.128

$^3F_4$ ——————— 12.365

$^3H_5$ ——————— 8.093
$^3H_4$ ——————— 5.552

$^3H_6$ ——————— 0.000
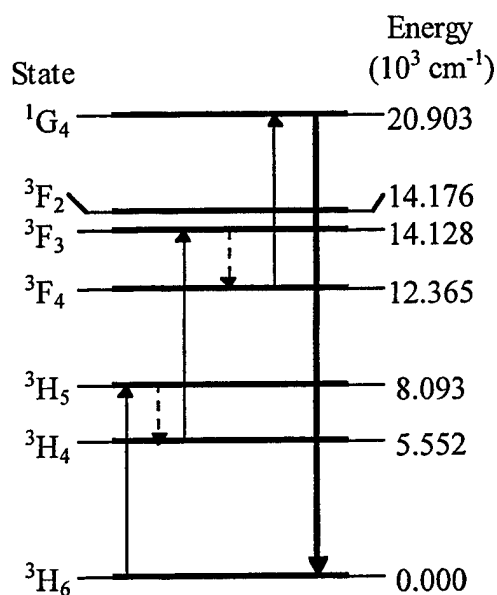
Figure 2-3. Dieke diagram of Tm^{3+} $4f$ states and single wavelength excitation scheme used to produce blue laser operation. Solid lines represent pump laser absorption, dashed lines are non-radiative decays, and bold arrow represents laser emission.

2.3 Alternative Excitation Scheme

To determine this alternative method for upconversion pumping, the first requirement is to remove the electrons from the ground ($^3H_6$) state (see Figure 2-3). The ground state absorption (GSA) spectra of Tm:ZBLAN fiber appears in Figure 2-4. As can be seen in the figure, the GSA at 1120 nm is less than 5 dB/km/ppm and improves to only around 10 dB/km/ppm at 1160 nm. Since the ground state
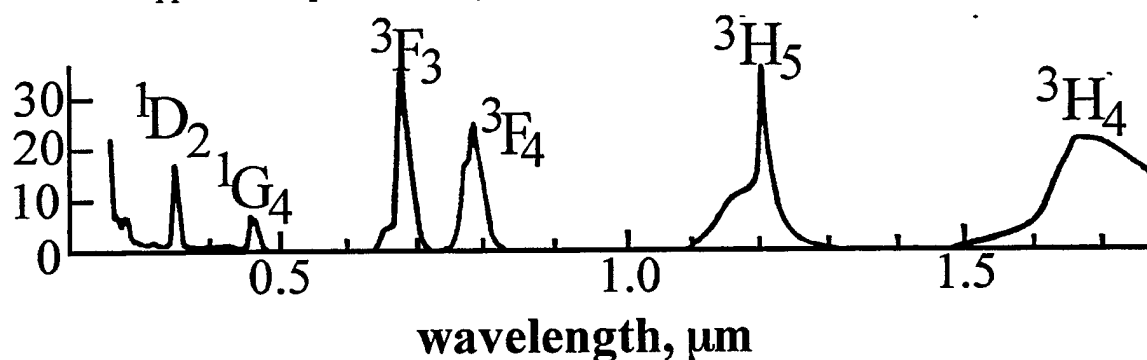
Figure 2-4. GSA spectrum of Tm:ZBLAN fiber.[1] The y-scale shows the absorption coefficient in dB/km/ppm. The $^3F_2$ absorption is unresolved from the $^3F_3$ peak near 680 nm.

is the terminating level for the laser transition ($^1G_4 \rightarrow {}^3H_6$), population inversion will be difficult to obtain and lower the slope efficiency of the laser when pumped with this single wavelength scheme.[1] Thus, we propose to use a 785 nm diode to excite the Tm ions out of the ground state.

Using this wavelength, we can now expect an absorption of >15 dB/km/ppm. This is a factor of one and a half to three better than the single IR source pumping scheme. While it appears that excitation to the $^3F_3$ level would be even more efficient, the width of the $^3F_4$ absorption is about 20 nm wider at 15 dB/km/ppm which relaxes the wavelength requirement of the pump laser and lowers its cost. Also, the use of 680 nm light to pump the $^3F_3$ level has been shown to increase the lasing threshold when laser emission at 800 nm ($^3F_4 \rightarrow {}^3H_6$) reaches threshold.[5] The use of a laser wavelength to pump a transition that can lase is not preferred, but if the pump light stimulates an excited electron to emit radiation, the emitted radiation would be at the pump wavelength. Thus, we would obtain an *increase* in pump power at 785 nm in the fiber allowing more efficient operation.

Once the Tm ion has been excited into the $^3F_4$ level, another laser wavelength is required to excite the ion to the upper laser level ($^1G_4$). This wavelength was determined by investigating the excited state absorption (ESA) spectra recorded by Grubb, et al. shown in Figure 2-5.[6] For this transition in the
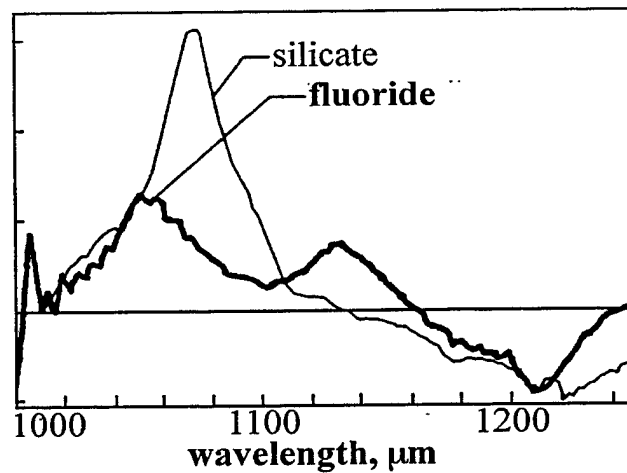
Figure 2-5. ESA spectra of Tm:ZBLAN.[6] Horizontal line denotes an even ratio of white light absorption between excited and unexcited fiber. Values above the horizontal, in increments of 0.5 where the horizontal is 1, show the increase in absorption when excitation is present while values below result from larger absorption when no excitation was used. Excitation was obtained with a 785 nm diode.

1120 - 1160 nm region, Tm ions in fluoride glass absorb light with a peak in the absorption around 1130 nm, and the peak of the GSA in this region (1160 nm) has practically no absorption! By investigating only two of the three absorptions involved in the single wavelength excitation scheme, we already have seen how sensitive the pump laser wavelength is on the performance of the blue laser. While data is not currently available on the other absorption process involved in the single wavelength excitation scheme, it is believed to only add more complexity and limitations to obtaining consistently efficient operation of a manufactured blue laser.

Since only this transition is being pumped by the second laser, we can match the laser wavelength to the peak in absorption. Hence, we chose to use an Nd:YLF laser at 1047 nm. At this wavelength, the ESA is slightly larger than that in the 1130 nm region, and we have approximately 20 nm around this wavelength that will give absorption that is better than that at 1130 nm (the wavelength often used to obtain blue laser operation).

2.4 Areas of Research

The development of a low power, low cost, compact, room temperature, blue laser source has been the goal of this project since its inception. Along with the modes of laser operation come numerous topics that need to be addressed and explored experimentally. This report will cover many of these topics. Initially, study of the gain material is required. While there is considerable documentation on the absorption and emission spectra of the rare earth ions, an investigation of these parameters is warranted to develop experimental and analysis skills. Subsequently, laser induced fluorescence is investigated along with the lifetimes of the fluorescence features. The proper assignment of these features allows knowledge of the energy level locations to be gained, and the fluorescence line shapes can be used to predict the emission and absorption cross sections as a function of wavelength -- something very important for theoretical modeling.

Since fiber is used as a gain material in this project, there are numerous possible experimental arrangements that can be used to obtain lasing using the dual wavelength excitation scheme. These possible cavity configurations will be addressed and compared by investigating a theoretical model of the small signal gain available from the fiber when the different cavity configurations are utilized. This model addresses the characteristics of CW operation as a function of the length of the fiber and predicts an optimal length of gain material to obtain the maximum small signal gain. A study of the fluorescence power emitted, related to the small signal gain, under dual wavelength pumping will be presented to show the true optimal length of fiber and deviations from the model will be discussed.

3. Methods, Assumptions, and Procedures

3.1 Gain Material Parameters

To understand the possible processes occurring in a laser, one must first investigate the material which will produce laser action. This investigation centers around the most important parameters required for lasing: dopant energy level locations, cross sections for absorption and emission, and decay lifetimes. All of these parameters can be determined from an analysis of laser-induced fluorescence. Toward that end, an experiment was set up to determine these parameters.

The end-light fluorescence experiment was arranged as shown in Figure 3-1. In this arrangement, an intra-cavity, line-selected Ar^+ laser is used as the excitation source. The monochromatic pump light was normally incident on a 50/50 beamsplitter with one of the beams
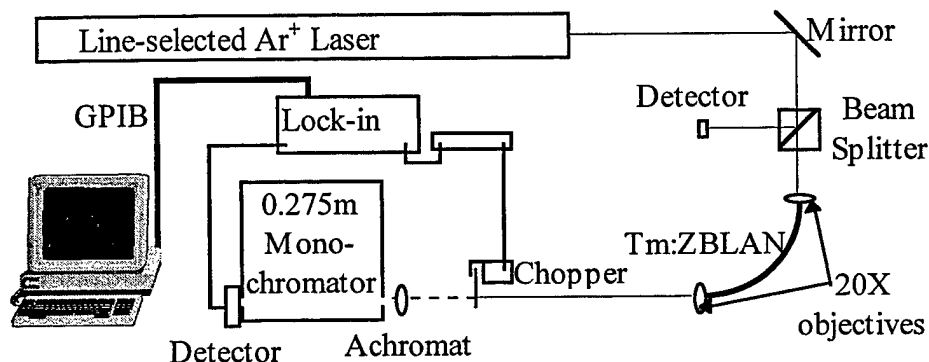
Figure 3-1. Experimental arrangement used to determine gain material parameters. To alleviate reabsorption effects, only 38 cm of Tm:ZBLAN was used.

being used to monitor the pump power and the other used to excite the Tm ions doped into fluorozirconate (ZBLAN) fiber. A 20X microscope objective was used to couple the pump light into the 38 cm Tm:ZBLAN fiber which has a dopant concentration of 1000 ppm. The emission from the fiber was collimated with another 20X microscope objective, which was corrected for chromatic aberrations, and then chopped at 400 Hz. A biconvex achromat was used to focus the emission into the 25 µm entrance slit of the monochromator. A variable exit slit was set at 50 µm and any signal passing through the exit slit was recorded with a Si or InGaAs detector. The signal was amplified with a digital lock-in amplifier and read to a computer via GPIB.

3.1.1 Energy Level Determination

Fluorescence spectra have been recorded previously for rare earth ions in silica and ZBLAN fiber as a precursor to the discussion of a fiber laser.[7,8] However, these spectra were not analyzed to determine the location of the energy levels. This analysis can be accomplished by

8

using analytical expressions previously documented which depend on the Slater integrals, F_2, F_4, F_6, and the spin-orbit constant, ζ.[9,10] This theory is based on the number of occupied $4f$ electron states of which trivalent Tm has 12.

Using the equations reported by Spedding, the energy level locations of the free ion of Pr^{3+} can be calculated.[11] A similar set of equations can be found in Dieke.[9] In all cases of rare earth ions, the $4f^N$ and $4f^{14-N}$ ions have the same theory with only the parity, and value, of the spin orbit constant, ζ, being different.[9] Hence, the theory discussed by Spedding can be used for Tm^{3+} since for Pr^{3+}, N = 2 and for Tm^{3+}, N = 12.

The electrostatic interaction in these ions involve no non-diagonal matrix elements, and the position of the various multiplets can be directly given by:[11]

$$^3H : E_1 = 0$$
$$^3F : E_2 = 15F_2 + 18F_4 - 273F_6 = 13.133F_2$$
$$^1G : E_3 = -5F_2 + 148F_4 + 91F_6 = 17.952F_2$$
$$^1D : E_4 = 44F_2 - 48F_4 + 728F_6 = 48.979F_2$$
$$^3P : E_5 = 70F_2 + 84F_4 - 127F_6 = 61.286F_2$$
$$^1I : E_6 = 50F_2 + 60F_4 + 14F_6 = 58.923F_2 \qquad (3.1)$$
$$^1S : E_7 = 85F_2 + 249F_4 + 1729F_6 = 149.461F_2$$

where the ^{2S+1}L portions of the state labels, i.e., ^3H, ^3F, etc. define the location of the Stark energy bands, the E_i label the energy bands in increasing order, and the F_i are the Slater integrals. The last column is the electrostatic interaction if a Coulombic field is assumed.

The spin-orbit interactions can be obtained by grouping all of the states with similar J values through:[11]

$$
\mathbf{J=6} \quad
\begin{array}{c|cc}
 & ^1I_6 & ^3H_6 \\
\hline
^1I_6 & I & \sqrt{6}\zeta \\
^3H_6 & \sqrt{6}\zeta & H+5\zeta
\end{array}
\qquad
\mathbf{J=5} \quad
\begin{array}{c|c}
 & ^3H_5 \\
\hline
^3H_5 & H-\zeta
\end{array}
$$

$$
\mathbf{J=4} \quad
\begin{array}{c|ccc}
 & ^3H_4 & ^1G_4 & ^3F_4 \\
\hline
^3H_4 & H-6\zeta & -2\sqrt{\tfrac{10}{3}}\zeta & 0 \\
^1G_4 & -2\sqrt{\tfrac{10}{3}}\zeta & G & 2\sqrt{\tfrac{11}{3}}\zeta \\
^3F_4 & 0 & 2\sqrt{\tfrac{11}{3}}\zeta & F+3\zeta
\end{array}
\qquad
\mathbf{J=3} \quad
\begin{array}{c|c}
 & ^3F_3 \\
\hline
^3F_3 & F-\zeta
\end{array}
$$

$$
\mathbf{J=1} \quad
\begin{array}{c|c}
 & ^3P_1 \\
\hline
^3P_1 & P-\zeta
\end{array}
\qquad (3.2)
$$

$$
\mathbf{J=2} \quad
\begin{array}{c|ccc}
 & ^3F_2 & ^1D_2 & ^3P_2 \\
\hline
^3F_2 & F-4\zeta & -2\sqrt{6}\zeta & 0 \\
^1D_2 & -2\sqrt{6}\zeta & D & 3\sqrt{2}\zeta \\
^3P_2 & 0 & 3\sqrt{2}\zeta & P+\zeta
\end{array}
\qquad
\mathbf{J=0} \quad
\begin{array}{c|cc}
 & ^3P_0 & ^1S_0 \\
\hline
^3P_0 & P-2\zeta & -4\sqrt{3}\zeta \\
^1S_0 & -4\sqrt{3}\zeta & S
\end{array}
$$

where the bold annotations denote the J value of the levels represented in the matrix, the underlined energy level labels, e.g., $^3H_6$, represent which column and row are associated with the contributions from that level and also shows which eigenvalue is associated with the level, the matrix entries are found as rows and columns to the left and below the underlined energy labels,

and the S, P, D, etc. denote the values of the electrostatic energy of the ^1S, ^3P, ^1D, etc. levels, respectively, found in (3.1).

To utilize this theory to determine the energy level locations, we begin with a list of radiative transition energies and the levels believed to be involved in the radiative transition. This data is labeled as $|Obs\rangle$. Initial guesses are required for the F_2 and ζ parameters with the initial guesses for the F_4 and F_6 calculated from the solution of a simultaneous equation set from (3.1). With these initial guesses, the eigenvalues of (3.2) are calculated. Next, the levels involved in each transition of $|Obs\rangle$ are used to calculate transition energies. With calculated transitions stored as $|Calc\rangle$, the sum square error of the calculated set is determined by:

$$SSE = \sum_{n=1}^{max}(|Obs\rangle - |Calc\rangle)^2 \tag{3.3}$$

where max is the number of transitions in $|Obs\rangle$. The routine continues by using a method of steepest decent to find the minimum SSE on the five dimensional surface described by F_2, F_4, F_6, ζ, and the SSE.

3.1.2 Cross Section Determination

Energy level locations are not the only data that can be obtained from the fluorescence spectrum. McCumber theory can be used to calculate one cross section from the other. The only assumption required is that thermal equilibrium within each manifold is reached before the state will decay.[12] From this theory, the cross sections are related by:[12]

$$\sigma_e(\nu) = \sigma_a(\nu)\exp\left\{\frac{\varepsilon - h\nu}{kT}\right\} \tag{3.4}$$

where $\sigma_a(\nu)$ and $\sigma_e(\nu)$ are the absorption and emission cross section, respectively, as a function of frequency, k is Boltzmann's constant, T is the temperature, and ε is the energy partition of the Stark levels involved in the transition. The equilibrium populations can be determined absolutely, provided ε is known, from:[12]

$$\frac{N_1}{N_2} = \exp\left\{\frac{\varepsilon}{kT}\right\} \tag{3.5}$$

where N_i is the equilibrium population of the ith level at T in the absence of optical excitation. If the positions of the Stark levels are known:[12]

$$\frac{N_1}{N_2} = \frac{1 + \sum_{j=2}^{n_1}\exp\left\{\frac{-E_{1j}}{kT}\right\}}{\exp\left\{\frac{-E_0}{kT}\right\}\left[1 + \sum_{j=2}^{n_2}\exp\left\{\frac{-E_{2j}}{kT}\right\}\right]} \tag{3.6}$$

where E_0 is the separation between the lowest component of each manifold, E_{ij} is the difference in energy between the jth and lowest component of level i, and n_i is the degeneracy of level i.

Since the electrostatic structure required for (3.6) is difficult to obtain, a simple phenomenological procedure can be used to yield ε by assuming that the Stark levels are equally spaced. Hence,[12]

$$E_{k\ell} = (\ell - 1)E_k \tag{3.7}$$

10

Now, ε can be determined by setting (3.5) equal to (3.6), and solving to yield:

$$\varepsilon = E_0 + kT \ln \left[\frac{\sum_{j=1}^{n_1} \exp\left\{\frac{-E_{1j}}{kT}\right\}}{\sum_{j=1}^{n_2} \exp\left\{\frac{-E_{2j}}{kT}\right\}} \right] \tag{3.8}$$

Since data for the energy band widths could not be found for Tm-doped ZBLAN, data collected for these widths for thulium ethylsulfate were obtained from Gruber and Conway.[13] While the host differs in this reference from the one investigated, it is believed that the difference in these widths is small compared to the total widths of the Stark multiplets.

With the investigation of fluorescence spectra as a function of wavelength, the cross section that can be obtained from the data is that of emission. Hence, (3.4) needs to be rewritten to allow its use in this context. This equation is rewritten as

$$\sigma_a(\lambda) = \sigma_e(\lambda) \exp\left\{\frac{1}{kT}\left(\frac{hc}{\lambda} - \varepsilon\right)\right\} \tag{3.9}$$

Desurvire presents a novel method to obtain the cross section for emission from the fluorescence spectrum by fitting the shape of the normalized fluorescence feature (normalized so that the maximum value is unity) with the sum of Gaussian line shapes.[14] While the line shapes have no physical meaning, they can be used to determine the wavelength dependence of the cross sections. Essentially, the fluorescence feature fitting function becomes:

$$I(\lambda) = \sum_i a_i \exp\left\{\frac{-(\lambda - \mu_i)^2}{2\delta_i^2}\right\} \tag{3.10}$$

where the (a_i, μ_i, δ_i) are the parameters of the fit. An absolute value for the cross section can then be obtained by normalizing the fitting function by the area of the curve and multiplying by:[14]

$$\sigma_e^{peak} = \frac{\langle\lambda\rangle^4}{8\pi n^2 c \tau \Delta\lambda_e^{eff}} \tag{3.11}$$

where $\langle\lambda\rangle$ is the mean wavelength of the transition, n is the refractive index of ZBLAN, c is the speed of light, τ is the measured lifetime of the transition, and $\Delta\lambda_e^{eff}$ is the effective line widths of the emission lineshape. Once the emission cross sections has been calculated, (3.8) and (3.9) are used to determine the cross sections for absorption.

3.1.3 Decay Lifetimes

To record the lifetimes of each state, some modifications were needed to the experimental arrangement depicted in Figure 3-1, and these modifications appear in Figure 3-2. The chopper is removed and a shutter is installed to control the exposure of the doped fiber to excitation. Instead of the lock-in amplifier an oscilloscope is used and averaged over repetitive fiber exposures to improve the signal to noise ratio of the detected decay.

From this setup, the rise and decay times could be determined by investigating different
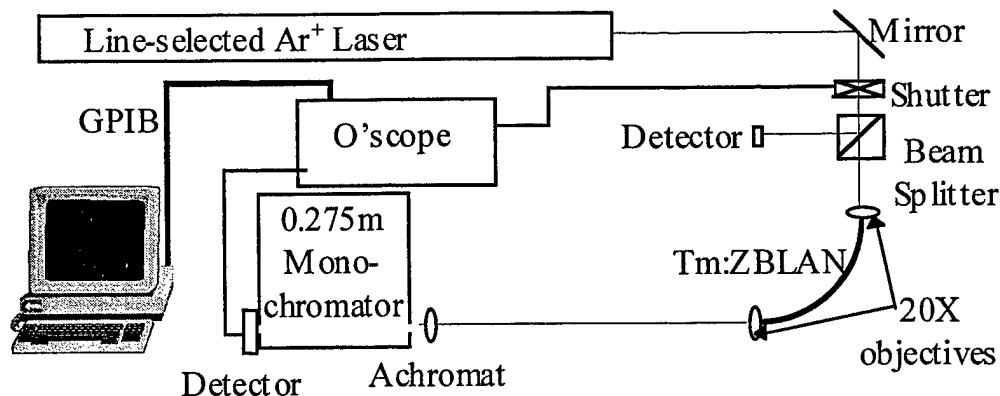
Figure 3-2. Schematic of experiment to determine the spontaneous radiative lifetimes of emission wavelengths in Tm:ZBLAN fiber. Laser output power was monitored by blocking the light prior to the fiber coupling objective, opening the shutter, and taking a reading on the detector. Traces were averaged on the oscilloscope over numerous exposures of the fiber, and the averaged scope traces were downloaded to computer for analysis.

regions of the shutter signal which is used to trigger the oscilloscope. To look at the rise times, which are important to aid in the proper spectral assignment of the emission, the region immediately after exposure began was investigated. Conversely, the trigger was changed to investigate the decay times by looking at the emission immediately after exposure of the fiber ceased. Care was taken to ensure that the transition being investigated was saturated before a decay time was measured, i.e., during exposure, the signal intensity had reached a maximum.

3.2 Small Signal Gain Calculation

To get an understanding of the gain available in the Tm:ZBLAN fiber and to determine the optimal length to make this fiber, a simple three-level upconversion laser system was modeled using the steady state approximation.

The numerical analysis of a fiber laser system can be very difficult without making some assumptions; in fact, no assumption-free closed form solution to the fiber laser exists. This model is no different in that there were numerous assumptions made to decrease the complexity of the model and still allow an investigation of the small signal gain, γ_o, and the effects of pump power and fiber length on γ_o, and the cavity configuration on the gain available above the threshold condition.

3.2.1 Initial Assumptions and Background

The initial assumptions were that the fiber was formed in a step index profile with a core radius, a, (area $= \pi a^2$) and a numerical aperture, NA.[15] Further, it was assumed that the dopant

12

radial profile was uniform and that all of the dopant was contained in the core of the fiber.[15] All of the fiber parameters where chosen to be invariant over the length of the fiber, and that all wavelengths propagating in the fiber where top hat modes, i.e., the radial and angular dependence of the power distribution of the pump and signal were assumed to be one in the core and zero in the cladding.[15] Finally, it was assumed that no stimulated emission could occur at any wavelength but the signal (blue) wavelength.

With the dual wavelength pumping scheme utilized in this investigation, the energy level diagram of Tm^{3+} $4f$ electronic states is simplified (see Figure 3-3). In this figure, the 785 nm laser radiation excites an electron from the $^3H_6$ to the $^3F_4$ state at a rate R_{12}. Once in this state, the electron has two possible avenues to leave this state. The first is by a spontaneous decay
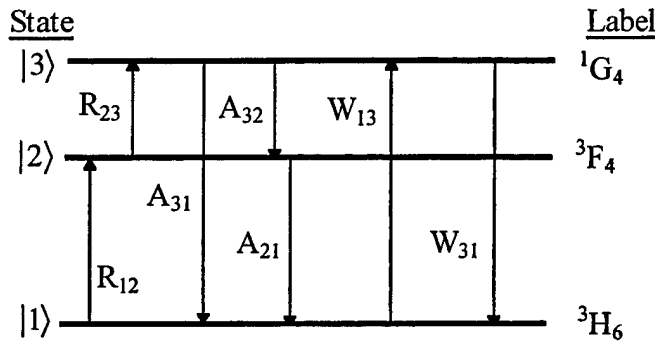
Figure 3-3. Tm^{3+} $4f$ electronic states used for dual wavelength pumping scheme. R_{ij} denotes the rate at which the j state is excited from the i state, W_{ij} denotes the emission/absorption rate from the i to j level, and the A_{ij} denote the spontaneous emission rate from i to j. All rates are in s^{-1}.

resulting in a photon with a wavelength near 800 nm at a rate A_{21}. The second, and desired, route is through the absorption of a photon of 1047 nm light which occurs at a rate R_{23}. Once excited to the $^1G_4$ state, the model assumed only three possible relaxation schemes. Two of these, A_{32} and A_{31}, involve the rate at which the excited electron can relax toward the ground state by the spontaneous emission of a photon around 1184 nm and around 480 nm, respectively. Note that the second spontaneous emission rate, namely A_{31}, is the emission from which lasing will begin when these photons are reflected back into the fiber core by dichroic mirrors. The third possible relaxation rate for the electrons is the stimulated emission rate, W_{31}. This is the rate at which spontaneous photons are replicated by stimulating the electron to relax to the ground state. Since this laser transition ($^1G_4 \rightarrow {}^3H_6$) is ground state terminated (GST) like the 1.55 μm erbium-doped silica transition, signal reabsorption can occur at a rate W_{13}. This reabsorption limits the length of the fiber gain material. The effect of the reabsorption is the increase of loss in the laser cavity. Thus, for a given 785 nm power, there will be a length of fiber which has the ground state depleted sufficiently throughout the fiber to limit the loss associated with W_{13}.

3.2.2 Rate Equation Model

From these possible transitions, coupled rate equations describing the population in each of the three levels can be written. These three equations plus the conservation of Tm^{3+} ions can shed light on the effects of pump power and fiber length to produce gain on the $^1G_4 \rightarrow {}^3H_6$ transition. These equations are:

$$\frac{\partial n_1(r,z)}{\partial t} = -\left[R_{12}(r,z) + W_{13}(r,z)\right]n_1(r,z) + \left[A_{21}\right]n_2(r,z) + \left[A_{31} + W_{31}(r,z)\right]n_3(r,z)$$

$$\frac{\partial n_2(r,z)}{\partial t} = \left[R_{12}(r,z)\right]n_1(r,z) - \left[R_{23}(r,z) + A_{21}\right]n_2(r,z) + \left[A_{32}\right]n_3(r,z) \qquad (3.12)$$

$$\frac{\partial n_3(r,z)}{\partial t} = \left[W_{13}(r,z)\right]n_1(r,z) + \left[R_{23}(r,z)\right]n_2(r,z) - \left[W_{31}(r,z) + A_{31} + A_{32}\right]n_3(r,z)$$

$$n_0 = n_1 + n_2 + n_3$$

where the A_{ij} terms give the rate (in s^{-1}) of spontaneous emission from the ith to the jth energy level, the n_i terms are the populations of the different states in Figure 3-3, n_0 is the total number of Tm ions doped into the fiber, and the R_{ij} and W_{ij} in (3.12) are given by:

$$W_{ij}(r,z) = R_{ij}(r,z) = \frac{\sigma_{ij} Q_{ij}(r,z)}{h\nu_{ij}} \qquad (3.13)$$

where h is Planck's constant, ν_{ij} is the frequency of the light generated from a transition between the ith and j^{th} levels, σ_{ij} is the cross section of the $i \rightarrow j$ transition, and:

$$Q_{ij}(r,z) = \frac{P_{ij}\psi_{ij}(r)\rho_{ij}(z)}{\pi a^2}. \qquad (3.14)$$

This function has the units of intensity ($W\ m^{-2}$) giving the units of R_{ij} and W_{ij} in s^{-1}. The functions that comprise $Q_{ij}(r,z)$ are P_{ij}, the power of the light corresponding to the $i \rightarrow j$ transition, the core radius, a, and the attenuation of the light, α, in the z direction (down the fiber):

$$\rho_{ij}(z) = 10^{\frac{-\alpha z}{10}} \qquad (3.15)$$

with the radial component of the intensity given by:

$$\psi_{ij}(r) = \begin{cases} 1 & for\ |r| \le a \\ 0 & for\ |r| > a \end{cases} \qquad (3.16)$$

since we have approximated all the modes as "top hats."

The cross section, σ, values in (3.13) can be determined from the method outlined in 3.1.2. However, since these cross sections can be difficult to obtain experimentally in fiber, the following relationship is used to approximate the cross section value when the lineshape cannot be determined:[16]

$$\sigma_{ij}(\lambda_o) = \frac{\lambda_o^4 A_{ij}}{8\pi c n^2 \Delta\lambda_{eff}} \qquad (3.17)$$

where $\Delta\lambda_{eff}$ is the effective linewidth of the emission (or absorption if σ_{ji} is being calculated).

14

The equations in (3.12) can be solved in the steady state, i.e., $\dfrac{\partial n_i(r,z)}{\partial t} = 0$, to obtain

equations for each $n_i(r,z)$. With a solution to equation (3.12) and the substitutions of equations (3.13) - (3.16) along with the values listed in Table 3-1, the population of each laser level can be numerically determined as a function of r and z. (Although for this calculation the r dependence

Table 3-1. Values used in theoretical model of small signal gain.

Coefficient	Value
A_{31} [16]	$600 \ s^{-1}$
A_{32} [16]	$138 \ s^{-1}$
A_{21} [16]	$665 \ s^{-1}$
σ_{31} [16]	$1.12 \times 10^{-25} \ m^2$
σ_{13} [16]	$7.72 \times 10^{-26} \ m^2$
σ_{32} [16]	$2.00 \times 10^{-25} \ m^2$
σ_{23} [16]	$2.00 \times 10^{-25} \ m^2$
σ_{21}	$1.26 \times 10^{-24} \ m^2$
σ_{12}	$1.81 \times 10^{-24} \ m^2$
α_{12} [17]	20 dB/km/ppm
α_{23} [18]	1.7 dB/km/ppm
$\alpha_{13} = \alpha_{31}$ [17]	7.5 dB/km/ppm
n_0	$1.54 \times 10^{25} \ m^{-3}$

is eliminated for $r \leq a$ since top hat modes are assumed.)

These functions can then be used to determine the inversion, Δn, the small signal gain, γ_o, per length and the gain, γ, for the optimal fiber length which are all functions of both IR pump powers. The inversion of a general laser system is given by:[19]

$$\Delta N = N_u - \frac{g_u}{g_l} N_l \tag{3.18}$$

where N_u and N_l are the populations and the g_u and g_l are the degeneracies of the upper and lower laser levels, respectively. Hence, the inversion of the upconversion pumped blue laser becomes:

$$\Delta n(r,z) = n_3(r,z) - \frac{9}{13} n_1(r,z) \tag{3.19}$$

where "9" and "13" are the degeneracies of the $^1G_4$ and $^3H_6$ levels, respectively.

The small signal gain, γ_o, per length can easily be calculated from:[19]

$$\gamma_o(\lambda_o, r, z) = \sigma_{31}(\lambda_o)\Delta n(r,z) \tag{3.20}$$

where the units of γ_o are m^{-1}. By supplying a small value of signal power to the model, approximately 1 nW, one can numerically determine the location of the greatest γ_o value as a function of z. This value denotes the fiber length for the maximum amount of gain before the effect of the W_{13} signal absorption rate begins to make the fiber lossy. This optimal length, d,

15

can then be multiplied by γ_o to yield the gain per pass, γ, from:[19]

$$\gamma(r,z) = \exp\{\gamma_o(\lambda_o,r,z)d\}$$ (3.21)

with units of dB.

3.3 Laser Experiments

3.3.1 Length Optimization

Since most of the research and development of blue fiber lasers has focused on the optimal length for the single wavelength excitation scheme, similar optimization work had to be accomplished for this project. The biggest hurdle to overcome in the creation of blue lasing from Tm:ZBLAN fiber is the optimization of the fiber length. This optimization is required since the lasing transition ($^1G_4 \rightarrow {}^3H_6$) is ground state terminated (GST). The effect of GST is the reabsorption of signal photons if the entire length of fiber is not excited from the ground state. Hence, a destructive test was used to evaluate the optimal length of fiber needed.

This experiment (shown in Figure 3-4) utilized a cut-back measurement to determine the fluorescence power of the 480 nm transition change as the fiber was shortened by 10 cm for each
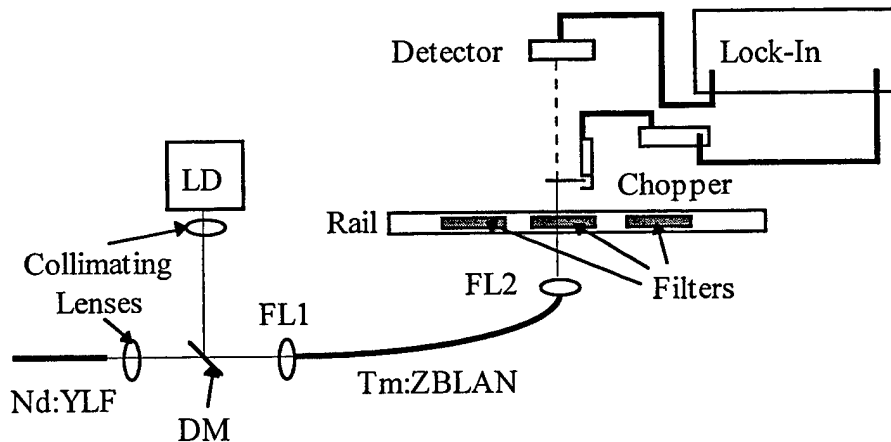
Figure 3-4. Cut-back experiment schematic. LD is a 785 nm laser diode, DM is a dichroic mirror, FL1 is a long-working distance, 20X objective that is corrected for chromatic aberrations, FL2 is a standard 20X objective, and the filters are placed on a rail to ensure similar orientation for each use.

new data point until the physical limit of the arrangement was reached at a fiber length of 0.4 m.

Light from the fiber-coupled Nd:YLF (at 1047 nm) and the laser diode (at 785 nm) was collimated and then combined with a dichroic mirror. This light was then incident on a specially designed objective which had a magnification of 20 and was corrected for chromatic aberrations. The light emitted from the fiber was collimated by a standard 20X objective, and filters were used to control the wavelength region passed to improve the signal to noise ratio. For further improvements to this ratio, lock-in detection was used.

16

3.3.2 CW Laser Configurations

Another significant consideration in the development of a laser is the amount of loss in the cavity. Since the gain material is fiber, and therefore flexible, numerous cavity shapes are possible. Also, the dual wavelength pumping scheme affords numerous methods by which to couple the light into the fiber.

The most feasible laser configurations are shown in schematic in Figure 3-5. There are four different configurations depicted in the schematic. In all configurations, the two diode lasers
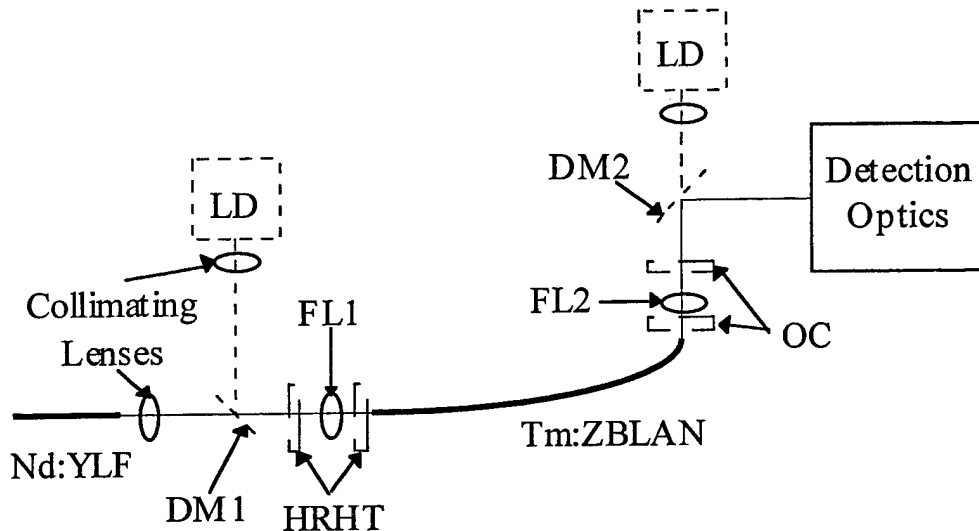
Figure 3-5. Possible cavity configurations and pumping schemes for dual wavelength pumped laser operation. The small dashes indicate items that could be moved/added to change from single end to dual end pumping where DM1 is a beam combiner and DM2 is a high reflector at the signal wavelength. The long dashes on the HRHT and output coupler denote the two possible locations for these mirrors. The detection optics are co-linear with the fiber end if DM2 is not used.

are coupled into a piece of Tm:ZBLAN fiber. Two mirrors, a high reflector, high transmitter (HRHT) which is ~99% reflective at 480 nm and ~99% transmissive at the pump wavelengths, and an output coupler (OC) which transmit ~99% of the pump laser wavelengths and is highly reflective at 480 nm, define the cavity of the laser. The exact reflectivity of the OC is another parameter that can be optimized by experimentation.

4. Results and Discussions

4.1 Gain Material Spectroscopy

Once the IR light has excited the Tm ions to the $^1G_4$ state, there are numerous routes by which the ions can relax to the $^3H_6$ state. Since the majority of the relaxations are radiative, we studied the fluorescence of the fiber after excitation by an argon laser operating at 457.6 nm arranged as shown in Figure 3-1. Other available lines from the argon shorter than 490 nm were observed to cause fluorescence in the fiber, however, we recorded upconversion fluorescence when using the 457.6 nm line for excitation (see Figure 4-1). The spectrum in Figure 4-1 was recorded with 60 mW of light incident on the lens used to couple light into the fiber. Since only
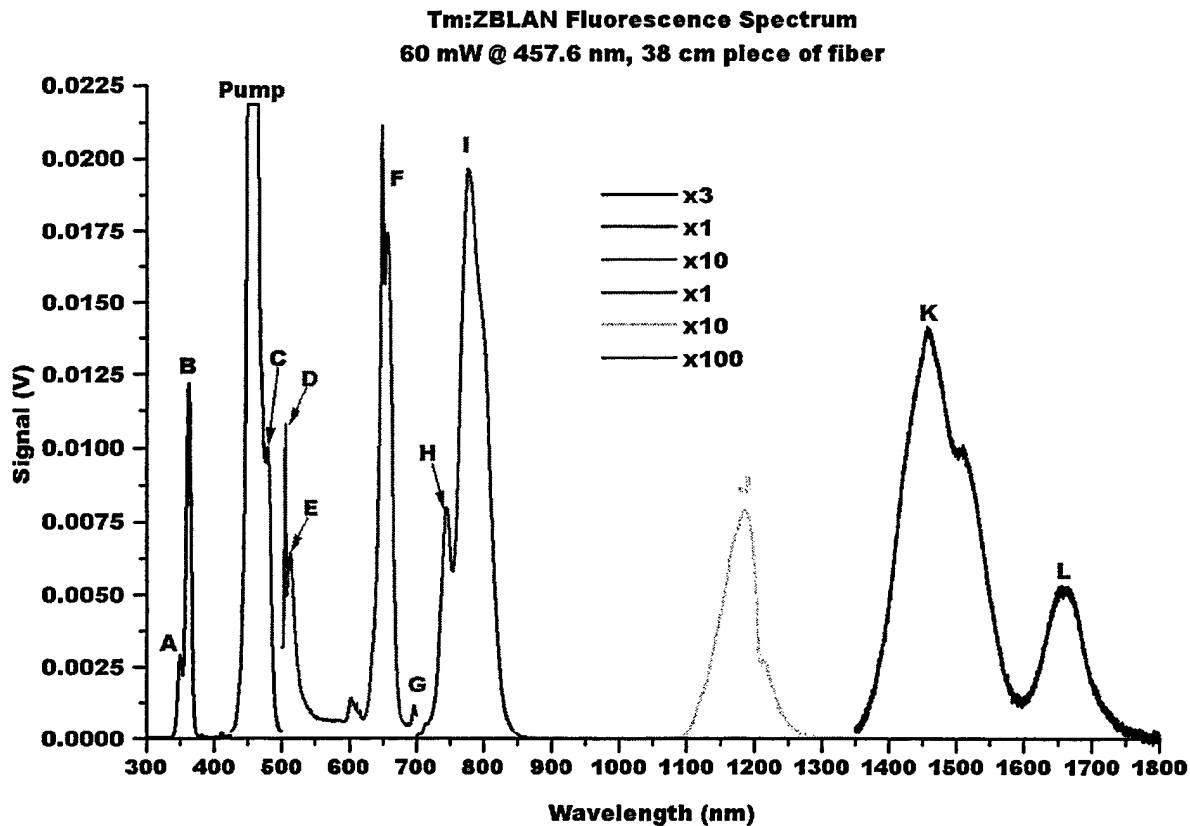
Figure 4-1. Laser induced, end light fluorescence of Tm:ZBLAN fiber. Separate transitions are labeled with letters. Features "A" and "B" result from an upconversion process. Fiber length was chosen to limit reabsorption effects, and 60 mW of pump power were incident on the coupling lens. Legend text shows the multiplicative factors for each spectral region.

50% of light incident on a coupling lens is typically launched into the fiber, we see upconversion processes, features "A" and "B", with only 30 mW of intra-fiber power. The transitions involved in each feature are listed in Table 4-1. All features which result from single pump

18

Table 4-1. Observed transitions in Tm:ZBLAN fiber. An asterisk (*) denotes transitions used to determine energy level locations. NA denotes an inability to obtain a measurement due to spectral blending.

Peak Label (Figure 4-1)	Transition(s)	Peak Wavelength (nm)	FWHM (nm)
a	$^1D_2 \rightarrow {}^3H_6$*	363.0	6.5
b	$^1D_2 \rightarrow {}^3H_4$	446.5	NA
c	$^1G_4 \rightarrow {}^3H_6$*	480.0	11.0
d	$^1D_2 \rightarrow {}^3H_5$	511.0	NA
e	$^1G_4 \rightarrow {}^3H_4$*	648.5	NA
	$^1D_2 \rightarrow {}^3F_4$*	657.6	NA
f	$^1D_2 \rightarrow {}^3F_2$*	746.5	NA
g	$^3F_4 \rightarrow {}^3H_6$*	807.0	30.0
h	$^1G_4 \rightarrow {}^3F_4$	1187.0	65.5
	$^3F_3 \rightarrow {}^3H_4$		
i	$^3H_5 \rightarrow {}^3H_6$	1229.0	NA
j	$^1D_2 \rightarrow {}^1G_4$	1294.5	16.5
k	$^1G_4 \rightarrow {}^3F_3$	1460.5	126.5
	$^3F_4 \rightarrow {}^3H_4$		
l	$^1G_4 \rightarrow {}^3F_2$	1627.5	NA

photon absorption agree with those published by Davey and France who used a pump wavelength which was not resonant with an excited state absorption in Tm.[20] As expected, there were a considerable number of transitions, and all of these exhibit the broad nature associated with Stark multiplet transitions in an anisotropic host.

4.1.1 Energy Level Calculation

These spectral features were used to determine the energy level locations of the Tm^{3+} $4f$ electronic states. These values were determined from a least squares fit of observed transitions to the theory first outlined by Dieke (discussed in 3.1.1) and appear in Table 4-2.[9]

Table 4-2. Energy level locations as determined from transitions noted in Table 4-1. All energy levels produce transitions within the spectral widths of the features in Figure 4-1.

Level	Energy (10^3 cm^{-1})
$^3P_1$	42.225
$^3P_2$	41.776
$^3P_0$	40.554
$^1I_6$	32.065
$^1D_2$	27.598
$^1G_4$	20.869
$^3F_2$	14.164
$^3F_3$	14.146
$^3F_4$	12.392
$^3H_5$	8.155
$^3H_4$	5.448
$^3H_6$	0.000
Fit Parameters	
Transitions	7
F_2	416.52
F_4	66.5459
F_6	5.32902
ζ	-1305.51
Standard Deviation (cm^{-1})	16.0749

Due to the significant blending of the spectral features in the infrared, only the visible and very near infrared transitions were used for the fit. Thus, only a small number of transitions could be used. However, the number of transitions is greater than the number of parameters and hence the fit produces viable energy level locations.

Considerable effort was put forth to verify the fitting routine. While raw data from other experiments was not available, previously published values for F_2 and ζ were available and used. It has been reported that the ratio of ζ/F_2 should be approximately six which results in the $^3F_4$ and $^3H_4$ levels being interchanged in Figure 2-3.[21] The initial guesses for the computer code were set to these values with the aforementioned levels interchanged in the assignment of the recorded transitions and a poor fit was obtained with fit parameters approximately equal to those in Table 4-2. With these transitions reassigned to the level locations in Figure 2-3, the locations and parameters do agree with those published by Spedding.[11]

4.1.2 Cross Section Calculation

The emission spectrum in Figure 4-1 was analyzed with the method described in 3.1.2, and Figure 4-2 shows plots of the emission and absorption cross sections of the 480 nm transition.

Emission Cross Section: $^1G_4 \rightarrow {}^3H_6$

σ_e (10^{-25} m^2)

Wavelength (nm)

(a)

Absorption Cross Section: $^1G_4 \rightarrow {}^3H_6$

σ_a (10^{-25} m^2)

Wavelength (nm)

(b)
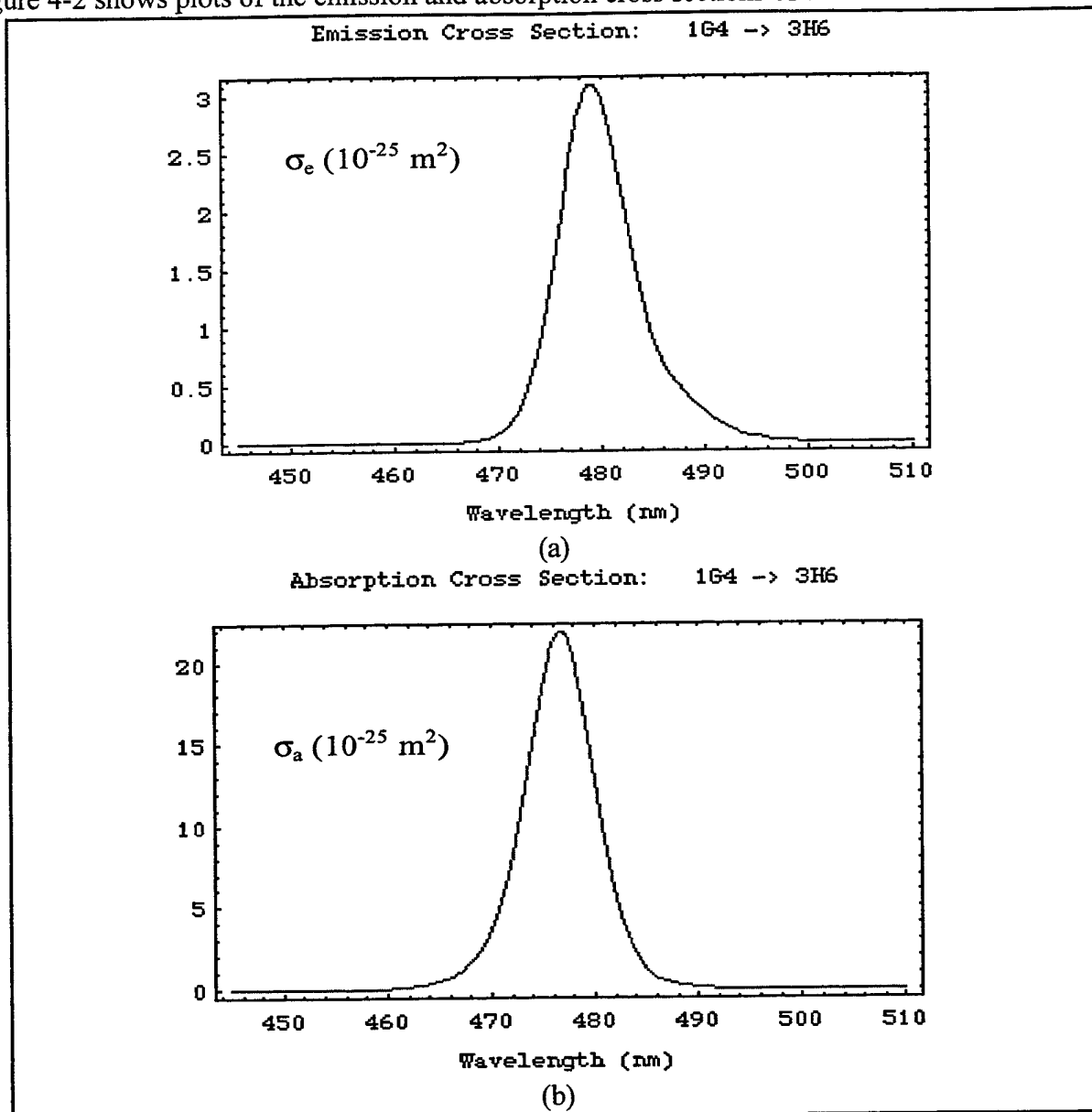
Figure 4-2. Sample emission and calculated absorption cross section for the $^1G_4 \rightarrow {}^3H_6$ transition in Tm:ZBLAN. The emission cross section (a) was determined by fitting the end light fluorescence signal in Figure 4-1 while McCumber theory was used to calculate the absorption cross section (b).

The actual values of the cross sections are approximately two orders of magnitude different than those published recently (reported as being 10^{-27} m^2 in magnitude).[22] This may be the result of an improper normalization or unit conversion in the calculation of the peak value of the emission cross section. Also, this reference shows the absorption cross section is lower than that of

21

emission. This may be correct, however, both calculations were based on the same theory and produce a factor of about seven for the ratio of the larger to smaller peak value. No information on where the other values for the emission and absorption cross sections were obtained for Ref. 22.

The pertinent Gaussian fit parameters and cross sections appear in Table 4-3. Unfortunately, all of the IR and some of the visible features suffer from the blending of multiple transitions and hence, functions fitting individual transitions could not be generated.

Table 4-3. Absorption and emission cross section values for some UV and visible transitions in Tm:ZBLAN. Gaussian fit parameters were used in Figure 4-2 to create a wavelength dependent expression for the emission cross section. McCumber theory was then used to determine the absorption cross section of each transition.

	Transition		
	$^1D_2 \rightarrow ^3H_6$	$^1G_4 \rightarrow ^3H_6$	$^1G_4 \rightarrow ^3H_4$
Lifetime (μs)	800	1240	1200
Absorption Cross Section			
Peak Wavelength (nm)	342.6	476.7	599.8
Mean Wavelength (nm)	342.6	476.6	595.0
Cross Section Peak (m^2)	$3.07424*10^{-23}$	$2.18521*10^{-24}$	$1.05585*10^{-22}$
Line Width (nm)	8.3	7.5	19.2
Emission Cross Section			
Peak Wavelength (nm)	362.5	479.0	648.4
Mean Wavelength (nm)	362.4	479.3	650.3
Cross Section Peak (m^2)	$1.91697*10^{-25}$	$3.09678*10^{-25}$	$4.53484*10^{-25}$
Line Width (nm)	6.4	7.8	18.6
Sum Square Error	0.00783	0.00708	0.00533

4.1.3 Decay Lifetime Measurements

Using the procedure established in 3.1.3, the decay lifetimes of the different spectral features in Figure 4-1 were determined using the experimental arrangement in Figure 3-2. Once again, spectral blending prohibited the collection data on many of the features. These blended features would show a multiple exponential decay with values that could not necessarily be attributed to a single transition. Hence, only the visible transitions were investigated.

The lifetime of the lasing transition was easily determined by detecting the 480 nm signal as a function of time after exposure by the 457.6 nm excitation. Figure 4-3 shows the signal averaged after 256 exposures for 100 ms with a 400 ms non-exposed time in between. Clearly

478.5 nm
Radiative Lifetime

Chi^2 = 0.00589

y0	0.197	±0
x0	0.848	±0
A1	0.86489	±0.023
t1	0.83962	±0.03194
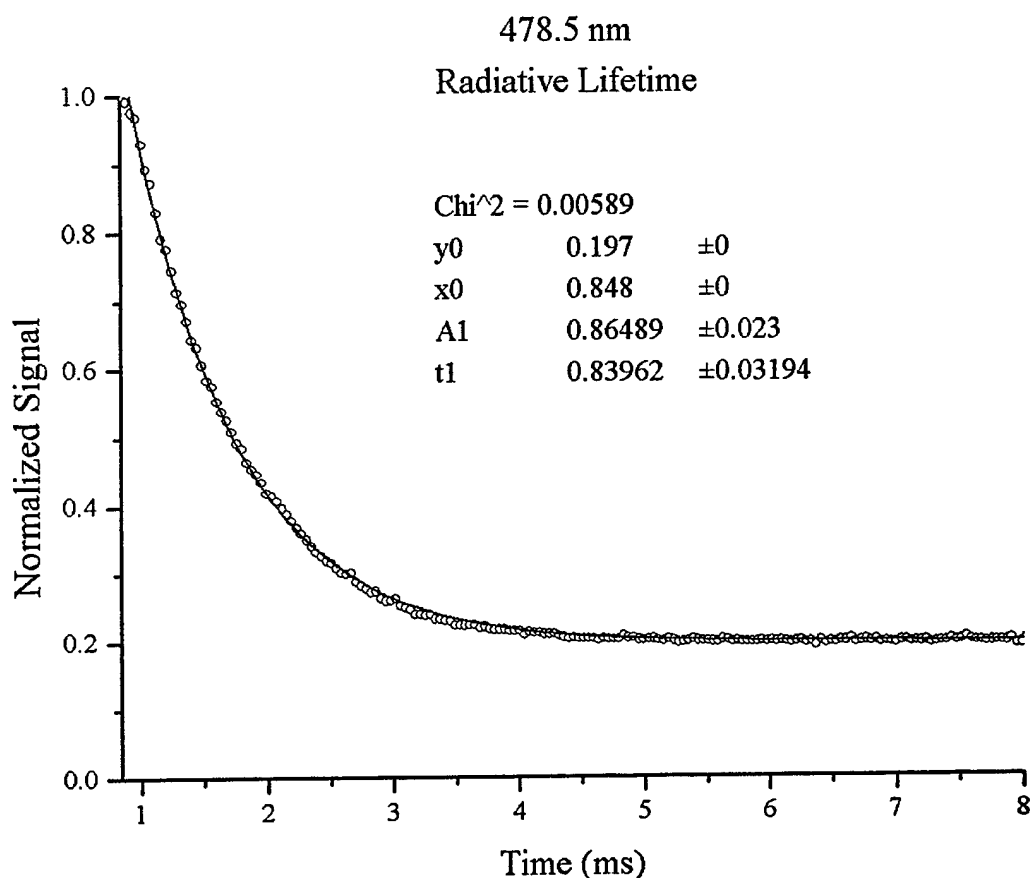
Figure 4-3. Spontaneous emission lifetime of the $^1G_4 \rightarrow {}^3H_6$ transition. Open circles are the experimental data points and the line is the exponential fit described by the parameters of equation (4.1).

this data is exponential and a fit to the data of:

$$y = y_0 + A_1 \exp\left\{\frac{x - x_0}{t_1}\right\}$$ (4.1)

shows little deviations from the exponential curve. This method found that the decay rate of the laser transition is (0.839 ± 0.032) ms. This and other values obtained from this experiment were similar to those presented in Sanz, et al.[23] However, there are some deviations which may be attributable to the exact composition of the host, the use of Tm:ZBLAN in fiber form for this lifetime measurement, and the experimental method used to collect this data.

4.2 Small Signal Gain

With GST being such a significant hurdle to the development of a laser, the computer code discussed in 3.2.2 was used to simulate the small signal gain as a function of fiber length.

While numerous approximations were made with this code it was believed to yield results to within a few tens of centimeters.

No data was available to verify this routine, however, by investigating the extremes of the pump powers one could get an idea if the code was operating properly. As expected, when the 785 nm power was extremely small, no significant gain was apparent at the signal wavelength. Similarly, no significant gain was apparent when the 1047 nm light was not used. Also, the output of the computer code generated the expected functional form for a GST transition (see Figure 4-4). At shorter lengths, a significant number of pump photons are not being absorbed by
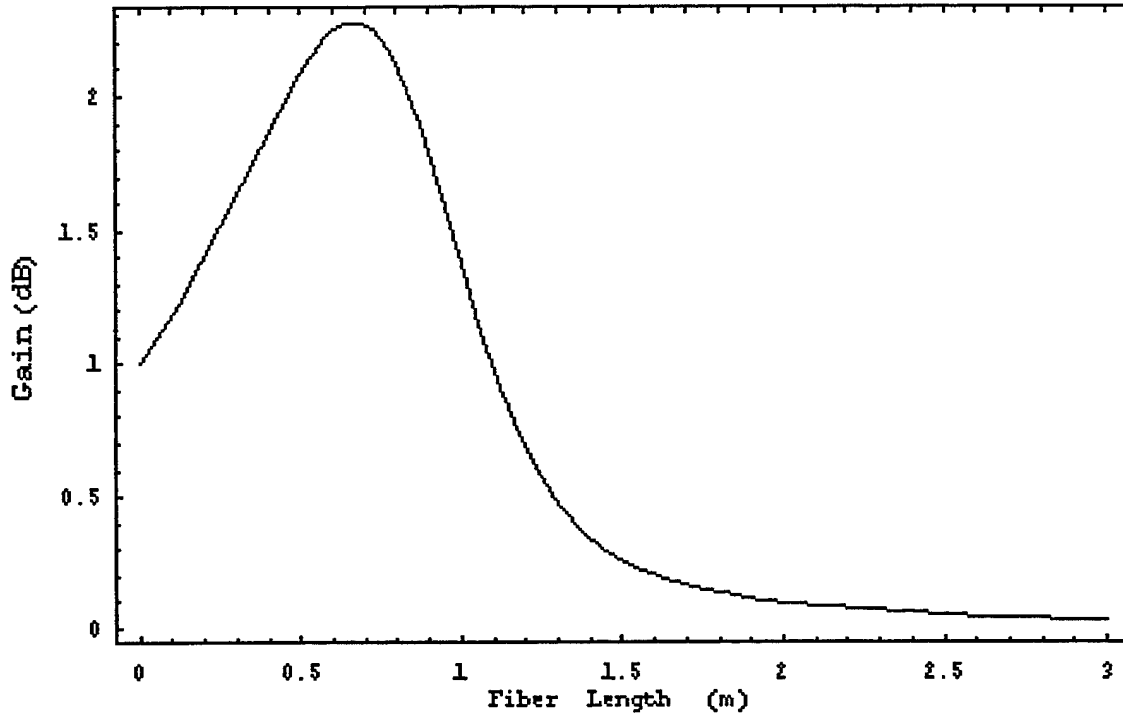
Figure 4-4. Gain from dual wavelength pumped blue fiber laser as a function of fiber length as predicted by the model described in 3.2.2.

the dopant in the fiber. An inversion has taken place, but the gain is low. At long fiber lengths, too few 785 nm photons exist to depopulate the ground state. Hence, the fiber turns lossy at the 480 nm wavelength, and the signal is significantly depleted; GST phenomena is occurring at lengths over 0.8 m. It is clear that the optimal gain is achieved at 0.7 m using pump powers of 35 mW and 250 mW for the 785 nm and 1047 nm, respectively.

4.3 Laser Results

While considerable delays in procurement and the unavailability to obtain some items kept this project from meeting all of the preliminary goals, this section will discuss the work completed by the end of this project. With the completion of the topics discussed in this section, only the physical alignment of the cavity should be required to obtain lasing at 480 nm, and this work will continue as the "Pulsed Blue Laser" project funded by Air Force Materiel Command.

4.3.1 Optimal Length

To verify that the results of the previous section were correct, a cut-back experiment, as depicted in Figure 3-4, was performed on 3 m of Tm:ZBLAN fiber. Both pump lasers were set to the maximum output power (70 mW and 500 mW) resulting in intra-fiber pump powers of 35 mW and 250 mW for the 785 nm and 1047 nm, respectively, assuming a coupling efficiency of 50%.

The data collected for the 480 nm fluorescence power, which has been corrected for the filter and detector responses, appears in Figure 4-5. The error bars on each data point arise from

480 nm Fluorescence Power
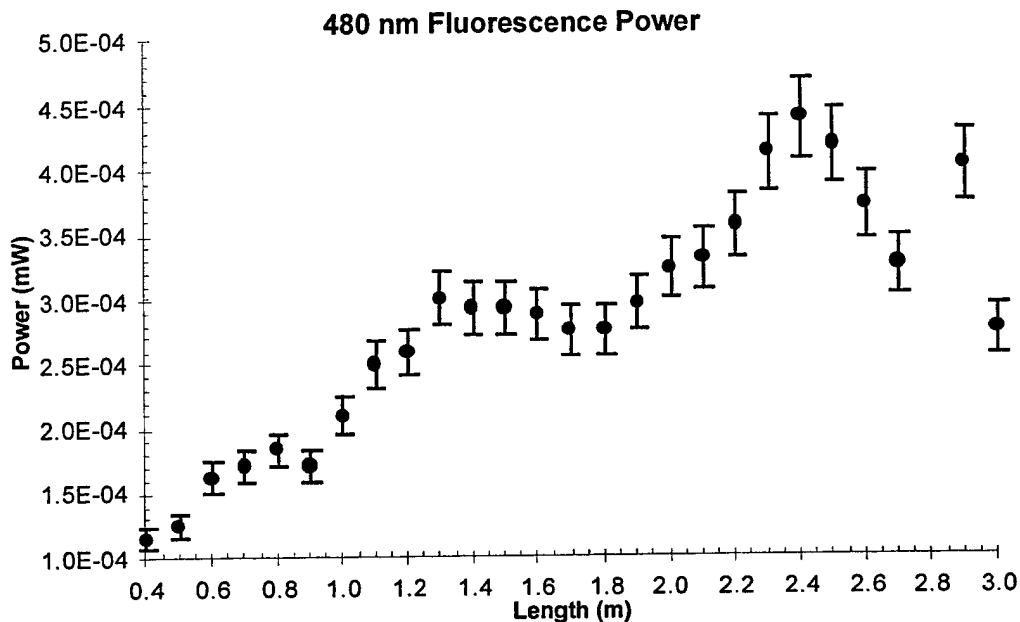
Figure 4-5. Fluorescence output power of 480 nm band as recorded through cut-back experiment. The error bars are estimated at 7% due to cleaving the fiber end after each cut. Due to this cleaving process, the fiber lengths are good to ±3 cm.

an assumed 7% loss in power due to the cleave at the output end of the fiber which had to be reaccomplished for each different fiber length. This error is believed to dominate the all other measurable errors possible in the data, e.g., the raw data errors were less than 1%. While not shown, the x data points have ±3 cm error in the length in an attempt to ensure suitable cleaves.

This figure shows a considerably different curve than that predicted by the model. Here, the maximum fluorescence power (which is related to gain) is optimal at 2.4 m. This can be explained by the number of transitions used in the model. Recall the model assumed all excited population was elevated to the $^1G_4$ level before relaxing down to ground with the emission of a 480 nm photon. Also, it was assumed that only 480 nm light was being produced. Clearly in the experiment, numerous possible deviations from the model assumptions can occur. First, the $^1G_4$ level can relax with the emission of a photon near 650 nm or 780 nm, and these transitions would compete for the population of the $^1G_4$ level. Second, the electron may not reach the $^1G_4$ level and

instead relax back down to ground from the $^3F_4$ level with the emission of a photon around 800 nm.

The model and the experiment show similar trends prior to and after the optimal value, but the experiment shows two steeply increasing sections followed by plateaus or losses in output power. Two possible explanations for these features that did not enter the model are the emission of other wavelengths (as described in the last paragraph) from the $^1G_4$ or $^3F_4$ levels, or a non-uniformity in the fiber dopant profile as a function of length. The former of these should be investigated in the future while the latter of these may be cost prohibitive.

4.3.2 Optimal Configuration

The optimal configuration of the blue fiber laser in this context implies that the system has limited intra-cavity losses and allows the blue laser output to be controllable with a minimal amount of optics. For the former requirement, one will investigate the components that have long dashed lines in Figure 3-5 (the mirrors), while the latter requirement implies a determination of which method of coupling the pump lasers will be most beneficial (the short dashed lines in Figure 3-5).

The best mode of operation for the blue laser output would be the configuration which places both pump lasers at the same end of the fiber with the HRHT mirror. In this manner, one optic can be used to control the laser emission exiting the cavity through the OC mirror. If the dual end pumped configuration were used, the optic at the output end of the fiber laser would be required to couple the pump light into the fiber *and* control the blue laser output. This would limit the efficiency of the laser and the controllability of the output emission. Since this project can be used for numerous Air Force signal processing applications, the control of the output emission is critical to allow the most cost efficient system.

To minimize the cavity losses, the gain values calculated from the model where used to investigate the effects of putting a *single* lens in the cavity. To date, multi-element microscope objectives have given the best coupling efficiencies, but the exact number of elements in a particular objective differs. While there is more loss from the microscope objectives, using the losses occurring from a single element show the effects of an intra-cavity optic.

To demonstrate the effect of the intra-cavity optic losses, the peak small signal gain calculated by the code described earlier was reduced by the losses associated with the two cavity configurations. The resulting gain available was then determined and plotted in Figure 4-6. Here the upper curve is the predicted peak gain obtained as a function of the intra-fiber 785 nm power when the cavity contains only the fiber, i.e., the mirrors are butted to the cleaved fiber ends and the pump light is coupled through mirror and into the fiber. The lower curve shows the same effect with a single element coupling lens intra-cavity. The difference curve represents the external minus the internal coupling value.

The two values shown above the difference curve represent the difference in gain from the two arrangements. At 35 mW of 785 nm power in the fiber, the gain is *increased* by 0.16 dB if

Cavity Configuration Comparison
R2 = 90%; 1047 nm power = 250 mW
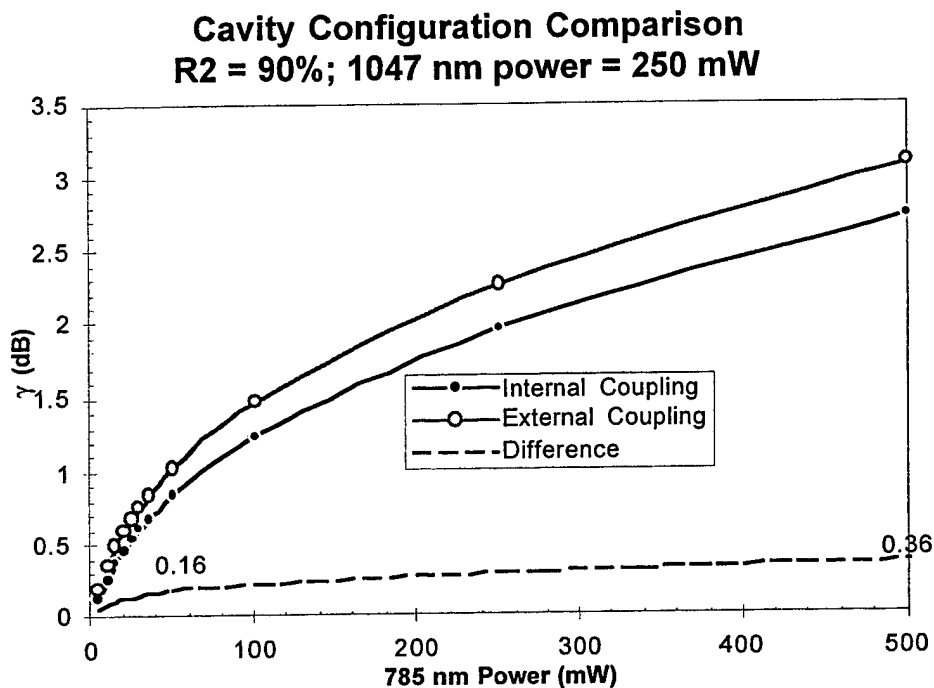
Figure 4-6. Comparison of two possible cavity configurations. The internal coupling configuration utilizes a single element optic between the fiber end and the mirror to launch light into the fiber while the external coupling uses the mirrors butted to the fiber ends and the lenses to couple the light through the mirrors and into the fiber.

the mirrors are butted to the fiber ends and the focusing lenses are external to the cavity. Similarly, if 500 mW of 785 nm was available, 0.36 dB more gain would be available with external coupling lenses. Recall that these differences were obtained by assuming a *single* element, yet no single element lens has been able to match the coupling efficiency of a microscope objective. However, objectives are typically multi-element and therefore would add 16% loss per element per objective. Thus, the losses obtained by placing three element objectives intra-cavity would reduce the gain considerably and thus would *not* be an optimal CW laser configuration. Therefore, an external coupling lens with both lasers coupled through the HRHT would be the optimal configuration.

5. Conclusions

Semiconductor diodes that emit in the blue region of the spectrum are not the only possible candidate for compact blue sources. Thulium-doped fluorozirconate, Tm:ZBLAN, fiber has lased at 480 nm with output powers greater than 100 mW when pumped with IR diodes.[4] This high output power was obtained with a single wavelength pumping scheme using light near 1130 nm. Since this single wavelength requires the absorption of three photons on three different transitions, the slope efficiency of the laser is low, and the effect of having a small deviation in the pump laser operating wavelength can drastically change the efficiency of the system. Hence, we propose a dual wavelength pumping scheme.

Because this excitation scheme uses two wavelengths for two different transitions, the wavelength of each pump laser can be selected to match the individual absorption maximum. Because the absorption (and emission) of light in Tm:ZBLAN fibers occurs over large wavelength regions, the wavelength requirements for the pump lasers are relaxed resulting in cheaper pump lasers. The wavelengths which optimize the $^3H_6 \rightarrow {}^3F_4$ and $^3F_4 \rightarrow {}^1G_4$ transitions are 785 nm and 1047 nm, respectively.

This report has presented numerous areas of research that have been completed to gain an understanding of the gain material and experimental procedures. These experiments included the collection of the laser induced fluorescence and spontaneous emission lifetimes of the fluorescence features. The fluorescence spectra was also used to determine the $4f$ electronic energy states in Tm:ZBLAN fiber. This analysis resulted in the energy level locations and parameters that describe the electronic processes of the Tm ion: the Slater integrals, F_2, F_4, and F_6, and the spin-orbit constant, ζ. These values, and the resulting energy level locations, agree with the recent publications on Tm:ZBLAN fiber lasers.[22,24]

The fluorescence spectra also allowed the determination of the absorption and emission cross sections in the visible region of the spectrum. This analysis was intended for use in a wavelength dependent computer model to determine the optimal pumping scheme for laser emission. However, the significant blending of the IR features (where upconversion pumping would take place) did not allow absolute measurement of the emission profile of individual transitions. Hence, a wavelength dependent model could not be created.

A simulation was created to obtain an approximation to the correct fiber length to achieve optimal small signal gain on the $^1G_4 \rightarrow {}^3F_4$ transition. This model, designed to be simple, made some approximations about the transitions involved in the emission of 480 nm photons. Due to these approximations, the model did not agree with the data obtained from a cut-back experiment which investigated fluorescence power as a function of the fiber length. This experiment showed that 2.4 m of fiber doped at 1000 ppm Tm concentration yields the highest fluorescence power (~450 nW) which is proportional to the gain available in the fiber. There were some interesting deviations in the expected trend for this data which may be explained through a spectral investigation of the 480, 650, and 800 nm wavelength regions for differing lengths of fiber.

Finally, several possible CW laser cavity configurations employing the dual wavelength pumping scheme where analyzed. The key factors in this analysis where the controllability of

the blue laser emission and minimization of the intra-cavity loss. This analysis showed that the single end pumped design will allow the most versatile control of the blue laser emission. Cavity losses will be diminished, available gain increased, and slope efficiency increased if the lenses used to couple the light into and capture the light emitted from the fiber are removed from the cavity to allow the mirrors to be butted against the cleaved fiber facets. While the difference in available peak gain was significant when only a single element coupling lens was introduced into the cavity, multi-element microscope objectives have shown the best coupling efficiencies causing the intra-cavity coupling arrangement to be even less attractive.

6. Recommendations

It is recommended that work continue on this program as the development of a compact, blue laser source will have significant impact in optical memory systems, inspections systems, and chemical agent detection to name a few applications. This two year effort began the investigation into blue fiber lasers at this laboratory, and now as the effort draws to a close, all of the required equipment for the initial laser development has arrived in-house.

As work presses onward, the first issue which should be addressed is the reason for the deviations from a steady increase of fluorescence power as a function of fiber length. It is believed that there are some competing transitions resulting in the plateaus and dips that deviate from the expected trend.

Upon determining the cause of these features, CW lasing should be attempted in the optimal cavity arrangement with 2.4 m of fiber as the gain material. This length of fiber, when excited with the dual wavelength pumping scheme, showed the largest fluorescence power. Hence, more spontaneous photons will be available to get the lasing process started.

After CW lasing has been achieved, a study of the blue emission parameters is recommended. These include, but are not limited to, the slope efficiency, the spatial mode, the threshold, the pump laser power effects on the threshold and slope efficiency, the maximum output power, the proper output coupler, the relative intensity noise (RIN), etc.

For the mode locked operation proposed for this effort, new devices must be grown. The most probable method to obtain these devices is through a contract with companies already growing devices which are optically active at 480 nm. Equipment to characterize these devices has already been purchased, and with the growth of these devices, this experiment should be built.

With devices that appear to have the proper recombination times, mode locked operation of the blue fiber laser should be attempted. Once achieved, similar measurements of the powers, noise, spectrum, spatial mode, etc. should be made.

7. References

[1] Davey, S.T. and P.W. France. *Br. Telecom. Technol. J.* **7** (1989).

[2] Bransden, B.H. and C.J. Joachain. *Physics of Atoms and Molecules*. Wiley & Sons, New York: 1991.

[3] Miniscalo, W.J. "Optical and Electronic Properties of Rare Earth Ions in Glasses",

[4] Sanders, S., R.G. Waarts, D.G. Mehuys, and D.F. Welch. *App. Phys. Lett.* **67** (1995).

[5] Tohmon, G., J. Ohya, H. Sato, and T. Uno. *Phot. Technol. Lett.* **7** (1995).

[6] Grubb, S.G., K.W. Bennett, R.S. Cannon, and W.F. Humer. *Electron. Lett.* **28** (1992).

[7] Percival, R. M., M. W. Phillips, D. C. Hanna, and A. C. Tropper. *J. of Quant. Elect.* **25**, 2119 (1989).

[8] Smart, R. G., J. N. Carter, A. C. Tropper, and D. C. Hanna. *Opt. Comm.* **82**, 563 (1991).

[9] Dieke, G. H. *Spectra and Energy Levels of Rare Earth Ions in Crystals*. Interscience. New York: 1968.

[10] Wybourne, B. G. *Spectroscopic Properties of Rare Earths*. Interscience. New York: 1965.

[11] Spedding, F.H. *Physical Review*. **58**, 255 (1940).

[12] Miniscalo, W. J., and R. S. Quimby. *Optics Letters*. **16**, 258 (1991).

[13] Gruber, J. B., and J. G. Conway. *Journal of Chemical Physics*. **32**, 1531 (1960).

[14] Desurvire, E. *Erbium-doped Fiber Amplifiers: Principles and Applications*. Wiley. New York: 1994.

[15] Digonnet, M. J. F., "Theory of Operation of Laser Fiber Devices",

[16] Duclos, F. and P. Urquhart, "Thulium-doped ZBLAN blue upconversion fiber laser: theory", *J. Opt. Soc. Am. B*, **12**, 709 (1995).

[17] Davey, S.T. and P.W. France, "Rare earth doped fluorozirconate glasses for fiber devices", *Br. Telecom. Technol. J.*, **7**, 58 (1989).

[18] Grubb, S.G., K.W. Bennett, R.S. Cannon, and W.F. Hunter, "CW Room-temperature Blue Upconversion Fibre Laser", *Electron. Lett.*, **28**, 1243 (1992).

[19] Verdeyen, J.T. *Laser Electronics, 2ed.* Prentice-Hall. Englewood Cliffs: 1989.

[20] Davey, S. T., and P. W. France. *Br. Telecom. Technol. J.* **7**, 58 (1989).

[21] Martin, W.C., R. Zalubas, and L. Hagan. *Atomic Energy Levels - The Rare-Earth Elements.* US Government Printing Office, Washington DC: 1978.

[22] Paschotta, R., P.R. Barber, A.C. Tropper, and D.C. Hanna. *J. Opt. Soc. Am. B.* **14**, 1213 (1997).

[23] Sanz, J., R. Cases, and R. Alcala. *J. Non-Cryst. Sol.* **93**, 377 (1987).

[24] Booth, I.J., C.J. Mackechnie, and B.F. Ventrudo. *IEEE J. Quant. Elect.* **32**, 118 (1996).

DISTRIBUTION LIST

addresses	number of copies
TODD E. WIEST ROME LABORATORY/OCPA 25 ELECTRONIC PKY ROME NY 13441-4515	6
ROME LABORATORY/CA CHIEF SCIENTIST 26 ELECTRONIC PKY ROME NY 13441-4514	1
ROME LABORATORY/SUL TECHNICAL LIBRARY 26 ELECTRONIC PKY ROME NY 13441-4514	1
ATTENTION: DTIC-OCC DEFENSE TECHNICAL INFO CENTER 8725 JOHN J. KINGMAN ROAD, STE 0944 FT. BELVOIR, VA 22060-6218	2
BALLISTIC MISSILE DEFENSE ORGANIZATION 7100 DEFENSE PENTAGON WASH DC 20301-7100	2
ROME LABORATORY/IMPS 26 ELECTRONIC PKY ROME NY 13441-4514	1
RELIABILITY ANALYSIS CENTER 201 MILL ST. ROME NY 13440-3200	1
ATTN: GWEN NGUYEN GIDEP P.O. BOX 8000 CORONA CA 91718-8000	1

```
AFIT ACADEMIC LIBRARY/LDEE                          1
2950 P STREET
AREA B, BLDG 642
WRIGHT-PATTERSON AFB OH 45433-7765


ATTN:  R.L. DENISON                                 1
WRIGHT LABORATORY/MLPO, BLDG. 651
3005 P STREET, STE 6
WRIGHT-PATTERSON AFB OH 45433-7707


WRIGHT LABORATORY/MTM, BLDG 653                      1
2977 P STREET, STE 6
WRIGHT-PATTERSON AFB OH 45433-7739



US ARMY SSDC                                        1
P.O. BOX 1500
ATTN: CSSD-IM-PA
HUNTSVILLE AL 35807-3801


NAVAL AIR WARFARE CENTER                            1
WEAPONS DIVISION
CODE 4BL000D
1 ADMINISTRATION CIRCLE
CHINA LAKE CA 93555-6100


SPACE & NAVAL WARFARE SYSTEMS                       1
COMMAND, EXECUTIVE DIRECTOR (PD13A)
ATTN:  MR. CARL ANDRIANI
2451 CRYSTAL DRIVE
ARLINGTON VA 22245-5200


CDR, US ARMY MISSILE COMMAND                        2
REDSTONE SCIENTIFIC INFORMATION CTR
ATTN: AMSMI-RD-CS-R, DOCS
REDSTONE ARSENAL AL 35898-5241


ADVISORY GROUP ON ELECTRON DEVICES                  1
SUITE 500
1745 JEFFERSON DAVIS HIGHWAY
ARLINGTON VA 22202


REPORT COLLECTION, CIC-14                           1
MS P364
LOS ALAMOS NATIONAL LABORATORY
LOS ALAMOS NM 37545
```

```
AEDC LIBRARY                                            1
TECHNICAL REPORTS FILE
100 KINDEL DRIVE, SUITE C211
ARNOLD AFB TN 37389-3211


AFIWC/MSY                                               1
102 HALL BLVD, STE 315
SAN ANTONIO TX 78243-7016


NSA/CSS                                                 1
K1
FT MEADE MD 20755-6000


PHILLIPS LABORATORY                                     1
PL/TL (LIBRARY)
5 WRIGHT STREET
HANSCOM AFB MA 01731-3004


ATTN:  EILEEN LADUKE/D460                               1
MITRE CORPORATION
202 BURLINGTON RD
BEDFORD MA 01730


OUSD(P)/DTSA/OUTD                                       2
ATTN:  PATRICK G. SULLIVAN, JR.
400 ARMY NAVY DRIVE
SUITE 300
ARLINGTON VA 22202

ROME LABORATORY/ERO                                     1
ATTN:  RICHARD PAYNE
HANSCOM AFB, MA   01731-5000


ROME LABORATORY/EROC                                    1
ATTN:  JOSEPH P. LORENZO, JR.
HANSCOM AFB, MA   01731-5000


ROME LABORATORY/EROP                                    1
ATTN:  JOSEPH L. HORNER
HANSCOM AFB, MA   01731-5000
```

ROME LABORATORY/EROC   1
ATTN: RICHARD A. SOREF
HANSCOM AFB, MA   01731-5000

ROME LABORATORY/ERXE   1
ATTN: JOHN J. LARKIN
HANSCOM AFB, MA   01731-5000

ROME LABORATORY/ERDR   1
ATTN: DANIEL J. BURNS
525 BROOKS RD
ROME NY   13441-4505

ROME LABORATORY/IRAP   1
ATTN: ALBERT A. JAMBERDINO
32 HANGAR RD
ROME NY   13441-4114

ROME LABORATORY/C3BC   1
ATTN: ROBERT L. KAMINSKI
525 BROOKS RD
ROME NY   13441-4505

ROME LABORATORY/OCP   1
ATTN: MAJOR GARY D. BARMORE
25 ELECTRONIC PKY
ROME NY   13441-4515

ROME LABORATORY/OCP   1
ATTN: JOANNE L. ROSSI
25 ELECTRONIC PKY
ROME NY   13441-4515

NY PHOTONIC DEVELOPMENT CORP   1
MVCC ROME CAMPUS
UPPER FLOYD AVE
ROME, NY   13440